Megahertz streak-mode Fourier domain optical coherence tomography

Rui Wang
Julie X. Yun
Xiaocong Yuan
Richard Goodwin
Roger R. Markwald
Bruce Z. Gao

Megahertz streak-mode Fourier domain optical coherence tomography

Rui Wang,[a] Julie X. Yun,[a] Xiaocong Yuan,[b] Richard Goodwin,[c] Roger R. Markwald,[d] and Bruce Z. Gao[a]
[a]Clemson University, Department of Bioengineering, COMSET, Clemson, South Carolina 29634
[b]Nankai University, Institute of Modern Optics, Tianjin, 300071, China
[c]University of South Carolina, Department of Cell Biology and Anatomy, Columbia, South Carolina 29208
[d]Medical University of South Carolina, Department of Regenerative Medicine and Cell Biology, Charleston, South Carolina 29425

Abstract. Here we present an ultrahigh-speed Fourier-domain optical coherence tomography (OCT) that records the OCT spectrum in streak mode with a high-speed area scan camera, which allows higher OCT imaging speed than can be achieved with a line-scan camera. Unlike parallel OCT techniques that also use area scan cameras, the conventional single-mode fiber-based point-scanning mechanism is retained to provide a confocal gate that rejects multiply scattered photons from the sample. When using a 1000 Hz resonant scanner as the streak scanner, 1,016,000 A-scans have been obtained in 1 s. This method's effectiveness has been demonstrated by recording *in vivo* OCT-image sequences of embryonic chick hearts at 1000 frames/s. In addition, 2-megahertz OCT data have been obtained with another high speed camera. © *2011 Society of Photo-Optical Instrumentation Engineers (SPIE).* [DOI: 10.1117/1.3593149]

1 Introduction

Much research has been devoted to increasing the imaging speed and resolution of optical coherence tomography (OCT). Although OCT with an A-scan rate of multimegahertz has been achieved using a swept light source,[1] it has not been achieved for the 800 nm regime.[2] In addition, the wavelength sweep range is narrow for presently available swept sources, resulting in limited axial resolution. Compared with swept-source OCT (SS-OCT), when the bandwidth or center wavelength is a concern, spectrometer-based Fourier domain OCT (FD-OCT) is more flexible in choice of the light source. For instance, supercontinuum light generated by photonic crystal fibers can cover either the 800 nm or the 1.3 μm regime.[3,4] However, in conventional FD-OCT, the A-scan rate is limited by the line-scan cameras [either a CCD type[5,6] or a CMOS type,[7] as shown in Fig. 1(a)]. An OCT A-scan is obtained by taking the Fourier transformation of the interference spectrum recorded on the camera sensor that is arranged as a one-dimensional array. Thus, the A-scan rate of an FD-OCT is equal to the line-scan rate of the camera that records and transfers the interference spectrum into the computer. Currently, the fastest line-scan camera (SPL4096-140k, Basler Vision Tec) can scan 140,000 lines in 1 s (each line includes 4096 pixels); even using a region of interest with 1024 pixels, the OCT A-scan rate will be less than 560,000 Hz. A state-of-the-art area-scan camera can achieve a higher data-acquisition rate than a line-scan camera can. For example, an area-scan camera (Fastcam SA5, Photron) can capture 7500 frames of two-dimensional images (1024 × 1000 pixels) in 1 s. If each interference spectrum is recorded by a line of sensor

comprised of 1024 pixels, 7,500,000 OCT A-scans can be obtained in 1 s when the exposure time is negligible. Thus, using high speed area-scan cameras allows for the development of a megahertz OCT.

In recently reported area-scan camera-based parallel spectral OCT,[8] an area-scan camera was used to record the spectra of the OCT signal in parallel by illuminating the sample with a line-light source. However, the crosstalk among different spatial image spots reduced both the signal-to-noise ratio (SNR) and the spatial resolution. This problem is also found in full field swept-source OCT (FF-SSOCT).[9]

Here, we report streak-mode Fourier domain optical coherence tomography (SM-FDOCT), a technique in which an area-scan camera is used instead of a line-scan camera to record the OCT spectrum. This SM-FDOCT retains the conventional point-scanning mechanism so that the small aperture of the single-mode fiber functions as a confocal gate for rejecting multiply scattered photons. While the probe beam is scanning the sample laterally, the corresponding OCT spectrum is physically scanned on the area-scan camera using a streak scanner, which can be, for example, a galvano mirror, a resonant mirror, a polygonal mirror, an acoustic- or electro-optic deflector. As shown in Fig. 1(b), pixels of the camera are illuminated by the OCT spectrum row by row in correspondence with each A-scan (depth profile) at different lateral positions.

2 Experimental Setup

2.1 *Light Source*

The streak-mode FD-OCT imaging system developed here is schematically shown in Fig. 2. A femtosecond (fs) laser (Tsunami, Spectra-Physics) provides a Gaussian-like spectrum at 830 nm with 80 fs pulse duration, corresponding to a spectrum

Address all correspondence to: Bruce Z. Gao, Clemson University, Bioengineering and Center for Optical Materials Science and Engineering, Clemson, South Carolina, 29364; Tel: 864-656-3311; E-mail: zgao@clemson.edu.
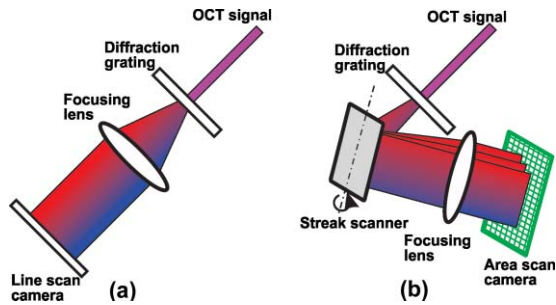
Fig. 1 Scanning mechanisms for (a) conventional FD-OCT and (b) streak-mode FD-OCT.

of 25 nm full-width-at-half-maximum (FWHM). A free-space isolator is used to block the back reflections. Then the laser beam passes a half wave-plate and a polarized beam splitter (PBS), successively. With the half wave-plate in rotation, the PBS plays the role of variable attenuator. The transmitted beam is coupled into a 50-m conventional single mode fiber (SMF), which has a mode field diameter of 5.6 μm. A broadened spectrum of 40 nm FWHM due to self-phase modulation[10–12] was obtained.

2.2 Interferometer

The SMF is connected to a high-power fiber circulator. The spectrally broadened light is redirected into the fiber circulator and then split into two beams by a 10/90 2×2 fiber coupler. The probe beam in the sample arm, extracted from the 90% port of the 2×2 fiber coupler by a collimator, is deflected by an X-Y scanner onto a sample via an achromatic lens, which provides a 1/e² spot size of 15 μm (beam waist radius w_0

= 7.5 μm). The reference beam in the reference arm, extracted from the 10% port of the 2×2 fiber coupler by a collimator, is focused on a reference mirror by an achromatic lens. The two beams, after interacting with the sample and the reference mirror, respectively, return to the 2×2 fiber coupler and combine to form an interference beam, the OCT signal, which is collected by the delivery fiber of the circulator. The polarization controllers in the two arms are adjusted to maximize the fringe visibility on the camera. A variable neutral density filter is placed in the reference arm to adjust the intensity of the reference beam for optimizing the system sensitivity.[13,14] A fiber-pigtailed diode laser, which has 1 mW output at 633 nm, is used as a marker laser to visualize the focal point of the probe beam within the sample.

2.3 Streak-Mode Spectrometer

After exiting from the output port of the circulator, the interference beam is collimated and then introduced into a streak-mode spectrometer, which is composed of an 1800-lines/mm transmission diffracting grating (Wasatch Photonics), a 4F configured lens pair, a 1000 Hz resonant scanner used as the streak scanner, a telescope unit, an achromatic focusing lens, and a high speed area scan CMOS camera (Y4, 1016×1016 pixels, 4000 f/s) from IDT.

The collimated interference beam, with a 1/e² diameter of 7.5 mm, enters the grating at an incident angle of 48 deg (in total $M = 20175$ grating lines are illuminated). The spectral resolution can be calculated by $(\delta\lambda)_{min} = \lambda_0/(mm)$, where λ_0 is the center wavelength of the source (here $\lambda_0 = 830$ nm), and m is the diffraction order (here $m = 1$), and thus $(\delta\lambda)_{min} = 0.041$ nm. Since the clear aperture of the resonant scanner is limited, the
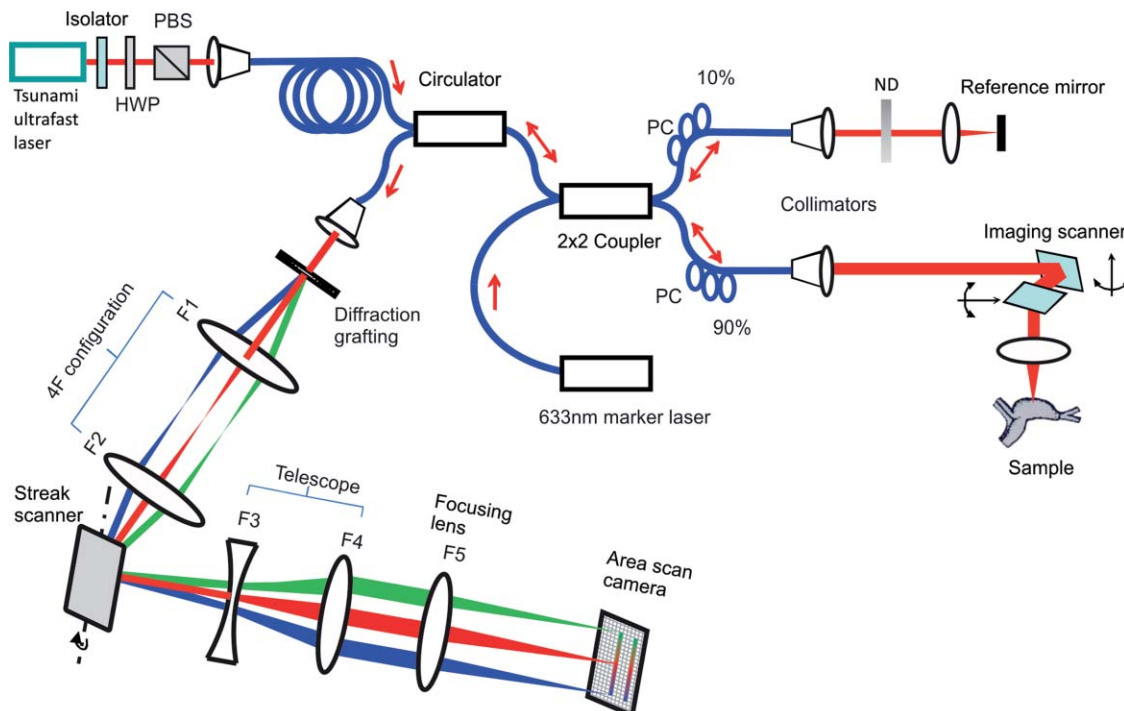
Fig. 2 Schematic of the streak-mode FD-OCT.

4F lens pair, which includes two identical achromatic lenses F1 and F2 ($f_1 = f_2 = 40$ mm), converts the diverging beam into a converging beam to make the beam fit the scanner's optical window. The grating is located at the front focal plane of F1, and the resonant scanner is placed at the back focal plane of F2.

The telescope, which is composed of a negative achromatic lens F3 ($f_3 = -40$ mm) and a positive achromatic lens F4 ($f_4 = 80$ mm), provides a 2:1 beam expansion ratio. This negative–positive lens-pair design reduces the length of the telescope and enables a large scanning angle range when the clear aperture of the lens is fixed. After expansion, the beam diameter is 15 mm. The focusing lens F5 ($f_5 = 150$ mm) is placed behind the telescope to focus the expanded interference beam into a sharp spectrum on the camera sensor. The numerical aperture is 0.05, resulting in a $1/e^2$ spot width of 10.6 μm, which is smaller than the pixel size (13.9 μm) of the camera. One row of the CMOS sensor (including 1016 pixels) detects a 80 nm bandwidth beam, and thus each pixel is separated by $\delta\lambda = 0.079$ nm, which is larger than the spectral resolution determined by the diffraction grating (0.041 nm). This spectral sampling interval results in a depth range of $Z_{RD} = 2.18$ mm, given by $Z_{RD} = \lambda_0^2/(4\delta\lambda)$.[15] Within a tissue with a refractive index of 1.34, the depth range is 1.63 mm.

The telescope plays an important role in the streak-mode spectrometer: since the clear aperture of the streak scanner is limited when high scanning speed is required, the beam diameter cannot be enlarged before passing the scanner. With the beam size being enlarged by the telescope located behind the scanner, the numerical aperture of the focused light is large enough to obtain a sharp spectrum on the sensor plane, maintaining the spectral resolution. In addition, the telescope reduces the paraxial angle of the interference beam incident on the focusing lens and thus decreases the effect of lens aberrations.

2.4 Synchronization of Scanners

Both the camera exposure and the streak scanning are synchronized with the B-scanning of the sample in the X direction. In detail, a NI 6733 board is used to generate a 1000 Hz sine wave as the voltage-angle input (VAI) signals for the X-scanner, another 1000 Hz sine wave is used as the external clock (EC) for the resonant scanner, and a 1000 Hz square wave is used as the exposure trigger (ET) signal for the camera. The control board of the X-scanner has an angle-voltage output (AVO) that is used as feedback signal indicating the true angular position of the scanner. The resonant scanner is phase-locked to the EC signal by the phase lock driver, which also has an AVO signal. For the X-scanner, there is a time delay between the VAI and the AVO signals. The time delay between the rising edge of the ET signal and the start of the exposure of the camera is much shorter than the X-scanner's delays and thus can be neglected. A multichannel oscilloscope is used to monitor the ET and AVO signals, and the phases of the VAI signal and the EC signal are adjusted to make sure that the X-scanner, streak scanner, and exposure of the camera are synchronized. During streak scanning, the focused spectrum line scans across the camera's sensor plane. Spectra corresponding to A-scans at different sample positions are recorded onto different rows of the area-scan camera. Each row of pixels matches the corresponding A-scan of the sample.

2.5 Effect of Streak Scanning

2.5.1 Mathematical model

Considering a single layer of scatterers, the sample's backscattering amplitude is simplified by $r(x, y, z) = r(x, y)\delta[z - z(x, y)]$. For a Gaussian beam with a large confocal parameter, the intensity profile can be expressed by:[16]

$$g(x, y, z) = \frac{1}{\pi w_0^2} \exp\left[-(x^2 + y^2)/w_0^2\right], \quad (1)$$

where w_0 is the $1/e^2$ spot radius of the probe beam. In conventional FD-OCT, a line scan camera is used to record the stationary spectrum line. The number of photoelectrons associated with fringes arising from the interference between the reference and sample beam can be given:[16]

$$N_{FDOCT}(k) \propto \int \text{rect}(t/T)dt \iint dx\,dy\, r(x, y)g(x - x_b, y - y_b)$$
$$\times \exp[-i2k(z - z_b)], \quad (2)$$

where (x_b, y_b) denote the transverse coordinate of the probe beam in the sample z_b denotes the longitudinal coordinate of the zero-delay point. In SM-FDOCT, the interference spectrum is scanned on the camera sensor. Considering that the focused spectrum line has a Gaussian profile in the direction perpendicular to the spectral line

$$h(\xi, k) = \frac{1}{\sqrt{\pi} w_1} \exp\left[-\xi^2/w_1^2\right], \quad (3)$$

where w_1 denotes the $1/e^2$ spot half-width ξ denotes the transverse coordinates of the focused spectrum line at the camera sensor, with ξ perpendicular to the spectral line. Correspondingly, the number of photoelectrons associated with an interference fringe received by each pixel of the camera can be calculated by:

$$N_{ST}(k) \propto \int dt \int_{-a/2}^{a/2} h(\xi + v_\xi t)d\xi \iint dx\,dy\, r(x, y)$$
$$\times g(x - x_b, y - y_b)\exp[-i2k(z - z_b)], \quad (4)$$

where a denotes the width of a camera pixel, and v_ξ denotes the moving velocity of the spectral line related to the camera sensor. Performing integration over the pixel width, we have:

$$N_{ST}(k) \propto \int H(t)dt \iint dx\,dy\, r(x, y)g(x - x_b, y - y_b)$$
$$\times \exp[-i2k(z - z_b)], \quad (5)$$

where

$$H(t) = \int_{-a/2}^{a/2} h(\xi + v_\xi t)d\xi. \quad (6)$$

Comparing Eq. (2) with Eq. (5), we can see the effect of streak scanning is merely a change of the time window from $\text{rect}(t/T)$ to $H(t)$, where T denotes the integration time of the line-scan camera in conventional FD-OCT; in SM-FDOCT, T is defined by $T = a/v_\xi$. Physically, $H(t)$ represents a prolonged integration time related to T. Examples of the prolonged integration time are shown in Fig. 3 for five different values of the pixel

Fig. 3 Prolonged integration time.

Fig. 4 Comparison of axial-motion-induced SNR drop between SM-FDOCT and conventional FD-OCT.
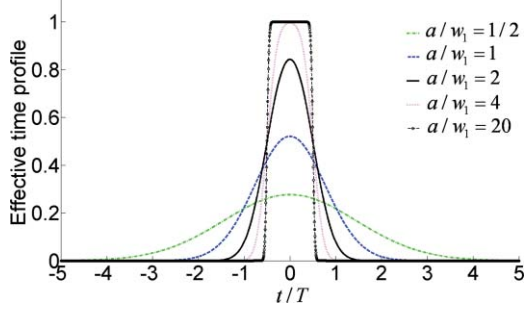
width normalized to the spot half-width of the spectrum line (a/w_1). Related to T, the effective integration time T_{eff}, which is defined as the $1/e^2$ width of $H(t)$, is prolonged by a factor of 5.7 for $a/w_1 = 1/2$; 3 for $a/w_1 = 1$; 1.85 for $a/w_1 = 2$; and 1.3 for $a/w_1 = 4$. When a/w_1 increases, $H(t)$ gradually approaches the rectangular function $\text{rect}(t/T)$ as shown in the case of $a/w_1 = 20$. For our setup, the designed a/w_1 was 2.6, which produced an integration time with a prolonged factor of 1.62.

It is notable that the area of the time profile is conserved, i.e., $\int H(t)dt = \int \text{rect}(t/T)dt$, although the temporal profile varies with different a/w_1. Physically, this means when a light beam with a constant power (not a time function) is introduced into a streak-mode spectrometer, the corresponding photon number for a single pixel will not change with a/w_1.

2.5.2 *Axial motion*

Considering the sample has an axial velocity v_z related to the probe beam, z_b is no longer a constant but is given by $z_b - v_z t$. For conventional FD-OCT, the axial motion produces a penalty in OCT signal intensity by a factor of $\sin^2(k_0 \Delta z)/(k_0 \Delta z)^2$ in the case of $|\Delta z| \ll z - z_b$, where $\Delta z = v_z T$.[16] For streak mode FD-OCT, similarly, Eq. (5) can be rewritten as:

$$N_{\text{ST}}(k) \propto \int H(t) \exp(-i2kv_z t)dt \iint dxdy\, r(x, y)$$
$$\times g(x - x_b, y - y_b) \exp[-i2k(z - z_b)]. \quad (7)$$

Performing time integration, we get:

$$N_{\text{ST}}(k) \propto D(k) \iint dxdy\, r(x, y)g(x - x_b, y - y_b)$$
$$\times \exp[-i2k(z - z_b)], \quad (8)$$

where

$$D(k) = \int H(t) \exp(-i2kv_z t)dt. \quad (9)$$

When calculating a complex-valued OCT A-scan profile by Fourier transforming Eq. (8) with respect to $2k$, the factor $D(k)$ can be approximated as a constant $D(k_0)$, in the case of $|\Delta z| \ll z - z_b$. Thus, Eq. (8) indicates that the axial motion produces a penalty in the OCT signal intensity by a factor of $D^2(k_0)$. Examples of the axial motion-induced SNR drop are calculated for 3 different values of pixel width a normalized to spot half-width w_1 of spectrum line and compared with the SNR drop in conventional FD-OCT (Fig. 4). In the case of the same
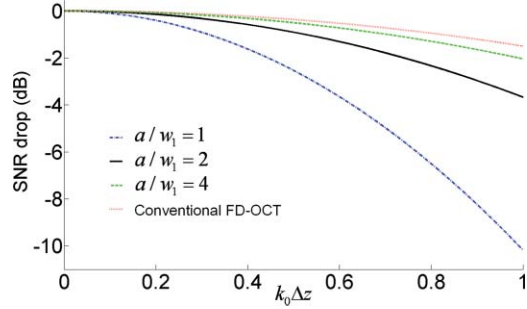
axial velocity v_z and T, SM-FDOCT has a larger SNR drop than conventional FD-OCT, especially when a/w_1 is small. This phenomenon can be described as: According to the discussion in Sec. 2.6.1, streak scanning introduces a prolonged integration time, and thus the fringe washout due to the continuous phase change of fringes is more severe than that seen in the case of conventional FD-OCT. When large a/w_1 is chosen (>2), this extra SNR drop is small in the case of $k_0 \Delta z \ll 1$. For our setup, the designed a/w_1 is 2.6, and the extra SNR drop is negligible when $k_0 \Delta z \ll 1$.

2.5.3 *Transverse motion*

Without loss of generality, we still assume that the sample is a single scattering layer moving at constant transverse velocity v_x related to the stationary probe beam. Thus, x_b is no longer a constant but is replaced by $x_b - v_x t$. Eq. (5) can be written as:

$$N_{\text{ST}}(k) \propto \int H(t)dt \iint dxdy\, r(x, y)g(x - x_b + v_x t, y - y_b)$$
$$\times \exp[-i2k(z - z_b)], \quad (10)$$

Performing time integration, we get:

$$N_{\text{ST}}(k) \propto \iint dxdy\, r(x, y)G_{\text{ST}}(x - x_b, y - y_b)$$
$$\times \exp[-i2k(z - z_b)], \quad (11)$$

where

$$G_{\text{ST}}(x, y) = \int H(t)g(x + v_x t, y)dt. \quad (12)$$

$G_{\text{ST}}(x, y)$ is an effective beam profile. For a random scattering sample, the speckle-averaged signal is proportional to $\int G_{\text{ST}}^2(x, y)dxdy$.[16] Thus, there is a SNR drop with the increasing velocity of the transverse motion. The amounts of the SNR drop with four different a/w_1 values are calculated and compared with that of the conventional FD-OCT in Fig. 5. The transverse displacement $\Delta x = v_x T$ is normalized to w_0. SM-FDOCT has a larger SNR drop than conventional FD-OCT, corresponding to the same $\Delta x/w_0$, especially when a/w_1 is small. This is because streak scanning leads to a prolonged integration time. When $\Delta x/w_0 = 1$, a/w_1 of 1/2, 1, 2, and 4 produce 3.56, 1.68, 0.76, and 0.45 dB, respectively, SNR decreases due to transverse motion; for conventional FD-OCT, the SNR decrease is 0.34 dB. In the case of $\Delta x/w_0 \ll 1$, the difference of the SNR drop between the streak mode and conventional FD-OCTs is small if the condition of $a/w_1 > 2$ is satisfied. For our setup,
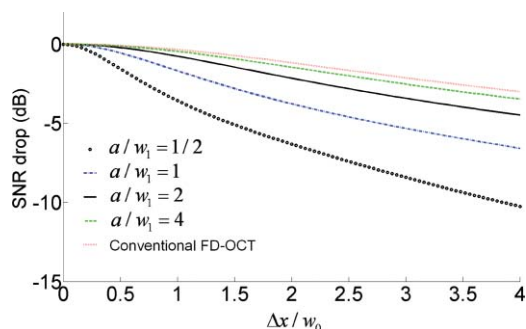
Fig. 5 Comparison of transverse-motion-induced SNR drop between SM-FDOCT and conventional FD-OCT.

the designed a/w_1 is 2.6; thus, the extra SNR drop is negligible in the case of small transverse motion.

3 Experiment

The X-scanner and the streak scanner were operated at 1000 Hz. Because the angular velocity of the resonant was a cosine function with time, v_ξ had larger values at the center and smaller values at the two ends of the scanning range, resulting in a nonuniform exposure of the entire camera sensor. To take full advantage of the dynamic range of the camera and avoid saturation, the range of the streak-scanning was set larger than the width of the entire sensor, and the sensing region occupied only the central 85% of the scanning range (approximately corresponding to the $[-58$ deg, 58 deg] phase range of the resonant scanner). The total scanning time for the entire sensor was about 320 μs and accounted for 64% of the unidirectional scanning. Thus, the overall duty cycle of the B-scanning was about 32%. In this case, the exposure level of pixels at two edges of the sensor was about 1.89 times that seen at the center. The camera, which could achieve 4000 frames/s at full resolution, was faster than the scanning frequency of the resonant scanner. During OCT imaging, the camera was operated at 1000 frames/s, with full resolution of 1016×1016 pixels, and the exposure time of the camera was set at 500 μs, which allowed integration only during unidirectional B-scans.

3.1 Sensitivity

3.1.1 SNR analysis

For a biomedical tissue sample, SM-FDOCT has an extra motion-induced SNR drop due to the prolonged integration time compared with conventional FD-OCT. For a stationary, mirror-like sample, the extension in integration time remains; however, the interference signal is invariant in phase and amplitude against streak-scanning, and thus there is no fringe washout; the sensitivity of the SM-FDOCT system can be theoretically calculated using a method similar to that used for conventional FD-OCT.[5]

$$\Sigma_{\text{ST}} = \frac{\Sigma N_s}{1 + N_{\text{el}}^2/N_{\text{ref}} + \alpha \left(f/\Delta v_{\text{pixel}} \right) N_{\text{ref}}}, \quad (13)$$

where ΣN_s is the sum of electrons over a line of camera pixels (corresponding to an A-scan) generated by the sample light returning from a 100% reflector, N_{el} is the electrical noise, N_{ref} is the electron number produced by the reference light,

α is a factor determined by the polarization degree of the light source ($\alpha = 1$ for unpolarized light and 2 for polarized light), f is the detection bandwidth, Δv_{pixel} is the spectral line width for a single pixel and can be calculated by $\Delta v_{\text{pixel}} = \Delta v/N$, where Δv is the effective spectral line width of the source,[14] and $N = 1016$ is the total number of camera pixels receiving a line of spectrum. However, for conventional FD-OCT, the detection bandwidth is given by $f = 1/(2T)$; for streak-mode FD-OCT, due to the prolonged integration time, the detection bandwidth is given by $f = 1/(2T_{\text{eff}})$. For a stationary mirror sample, both sample power P_s and reference power P_r are constant. Since $\int H(t)dt = \int \text{rect}(t/T)dt$ (Sec. 2.5.1) for streak-mode FD-OCT, we get $\Sigma N_s = \rho\eta P_s T/(hv_0)$ and $N_{\text{ref}} = \rho\eta P_r T/(hv_0 N)$, where $\rho = 64\%$ is the spectrometer efficiency, $\eta = 30\%$ is the quantum efficiency of the camera, h is Planck's constant, and v_0 is the center frequency of the light source. After propagating in the long single-mode fiber, the light can be treated as an unpolarized light ($\alpha = 1$). Here, $\Delta v_{\text{pixel}} = 17.9$ GHz.

The main noise sources in each pixel include the shot noise N_{sh}, the electrical noise N_{el}, and the relative intensity noise N_{RIN}, all measured in number of electrons. The full well capacity of the Y4 camera is 40,000 electrons. To avoid the saturation of pixels at the two sides of the sensor, the reference light is adjusted to allow about 40% camera saturation at the center (around the 508th A-scans); thus, for each pixel, N_{ref} is about 16,000 electrons and the number of shot noise photoelectrons is 126.5, given by $N_{\text{sh}} = N_{\text{ref}}^{1/2}$; the electrical noise, including the read-out noise, the dark current noise, and the digitization noise, is found to be $N_{\text{el}} = 70.9$ electrons. The RIN noise is given by $N_{\text{RIN}} = \left(f/\Delta v_{\text{pixel}} \right)^{1/2} N_{\text{ref}}$.[5] At the center of the sensor, the streak scanning velocity v_ξ is 52.1 m/s, thus, $T = a/v_\xi$ is 0.267 μs; because of the prolonged integration factor of 1.62 in the case of the designed $a/w_1 = 2.6$, the effective integration time T_{eff} is about 0.43 μs, resulting in a 1.16-Mhz detection bandwidth. Thus, the RIN noise is 128.6 electrons, slightly larger than the shot noise. Therefore, for each pixel, the total noise power $N_{\text{noise}}^2 = N_{\text{sh}}^2 + N_{\text{el}}^2 + N_{\text{RIN}}^2$ is 2.35 times the shot-noise limit. A total sample power of 37.5 mW returning from a gold-mirror sample was measured at the output fiber tip of the interferometer. Equation (13) predicts a sensitivity of 95.3 dB for the A-scans around the central region of the camera. For A-scans at two sides, $T = a/v_\xi$ is about 0.503 μs, corresponding to an effective integration time T_{eff} of about 0.81 μs, and, thus, the RIN noise is 177.6 electrons ($N_{\text{ref}} = 30,240$ electrons). As a result, the total noise is 2.21 times the shot-noise limit. Equation (13) predicts a sensitivity of 98.3 dB.

3.1.2 Experimental measurement of SNR

To measure the sensitivity of the system, we placed a 3 OD neutral density filter (total attenuation: –60 dB) into the sample arm and used a gold mirror as the sample. The X- and Y-scanners were not operated. The sensitivity was calculated by measuring the SNR (SNR = $10 \log_{10}[S_{\text{peak}}^2/N_{\text{var}}]$, where S_{peak} and N_{var} represent the signal peak of the mirror and noise variance, respectively) and adding 60 dB to this value. Figure 6 shows the sensitivity distribution along the B-scan when the mirror was located at a depth of 450 μm. The data demonstrated that the sensitivity of ~95 dB was measured at the center of the B-scan,
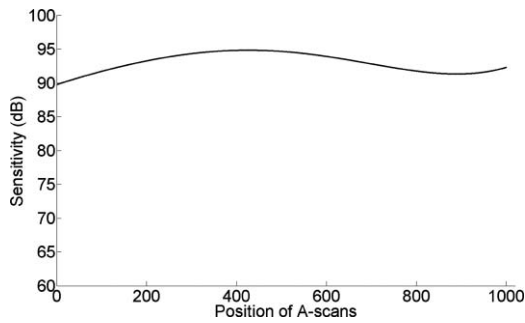
Fig. 6 Sensitivity distribution of the SM-FDOCT system.

in agreement with the theoretically expected value 95.3 dB. At two sides of the B-scan, >90 dB sensitivity was measured, but lower than the theoretically expected value. This might be because lens aberrations were more severe at two sides than at the center, which could result in degraded spectrometer resolution and fringe visibility; thus, there was an extra SNR decrease at two sides of the B-scan. This issue might be addressed by aberration correction. Since the resonant scanner was thin, another possible reason was the mirror's wobbling and deformation at two ends of the scanning range, where it had larger angular acceleration and thus distorted the wavefront and introduced extra aberrations; this could be improved by using a more rigid streak scanner (i.e., a polygonal scanner).

3.2 OCT Imaging

To demonstrate imaging capability of the proposed SM-FDOCT, we imaged several biomedical samples using our SM-FDOCT.

3.2.1 In vitro imaging of an onion sample

An onion sample was imaged using this OCT system. The result is shown in Fig. 7.

3.2.2 In vivo imaging of a developing embryo chick heart

To demonstrate the dynamic imaging capability, our SM-FDOCT was used to image the heart outflow tract (OFT) of HH19 stage chick embryos. Fertilized white leghorn eggs were incubated at 38.2 °C until they reached the HH19 stage. A window was open at the air sac end of the shell and a part of
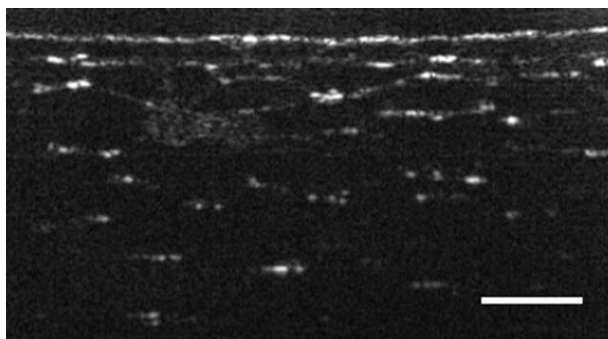
Fig. 7 SM-FDOCT image of an onion sample. The scale bar is 200 μm.
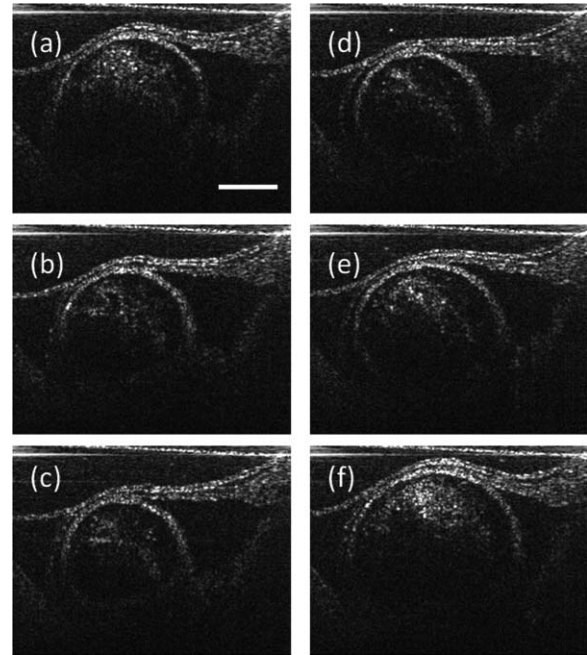
Fig. 8 SM-FDOCT image sequence in a single heart stroke of an HH19 chick embryonic heart at 1000 frames/s (Video 1): (a) beginning of the systole (Video 2); (b) mid-systole; (c) end of the systole; (d) beginning of the diastole (Video 3); (e) mid-diastole; and (f) end of the diastole. Scale bar: 200 μm. Video 1 (MPEG, 6.6 MB) [URL: http://dx.doi.org/10.1117/1.3593149.1]; Video 2 (MPEG, 2.0 MB) [URL: http://dx.doi.org/10.1117/1.3593149.2]; Video 3 (MPEG, 3.6 MB) [URL: http://dx.doi.org/10.1117/1.3593149.3].

the chorionic membrane was carefully removed to enable optical access to the embryo. During OCT imaging, the embryo was left in the shell. To maintain a constant temperature, about three quarters of the egg was dipped into a 37 °C custom-made water-jacketed incubator with a temperature control system including a heater and a temperature feedback unit. The whole water-jacketed incubator was placed on the stage of the OCT system.

To image the OFT, the height of the OCT probe was adjusted by a vertical translation stage to bring the chick heart in focus. About 30 mm working distance between the probe and the egg allowed us to see the transverse position of the focal point with the help of the 633 nm marker laser, which shares the same OCT probe with the imaging broadband source centered at 830 nm. A sequence of 2000 cross-sectional images across the OFT were acquired in 2 s. The results are shown in Fig. 8 and Video 1. A systole period of 120 ms is displayed by Video 2, and a diastole period of 220 ms is displayed by Video 3.

4 Discussions

We noticed that the strong sample power might exceed the laser exposure safety standard, depending on the scanning protocol, although the safety standard for a chick heart is unknown. A multiple-channel design, using multiple well-separated probe beams,[1] can reduce the light-induced damage for biomedical samples. Furthermore, for a system with low-duty cycle, the light can be blocked by a high speed shutter (i.e., an electro-optic

Table 1 Comparison of different streak scanners.

Type of scanner	Clear aperture (45 deg incident angle)	Repetition rate	Angular scan range (optical)	Total scanning speed
Galvano mirror	10 mm	500 Hz	5 deg (unidirectional)	2500 deg/s
Resonant mirror	10 mm	1000 Hz	16 deg (unidirectional)	16,000 deg/s
Polygonal mirror[a]	10 mm	2000 Hz	24 deg (at 50% duty cycle)	48,000 deg/s

[a]A polygonal mirror with 15 facets and 150 mm diameter, rotating at 8000 rpm.

modulator) during the dead time. For instance, in our setup, the duty cycle is 32%, thus, the total exposure energy for biomedical samples can be reduced by ∼3 times with a shutter.

A problem with this resonant scanner-based SM-FDOCT is nonuniform exposure that occurs because of the velocity of the streak scanning is a cosine function of time. To avoid saturation of the camera, the scanning range of the resonant scanner was set larger than the width of the sensor; however, this compromise resulted in a reduced duty cycle (32%). If a galvano scanner is used as the streak scanner, linear streak scanning can be held in most of the scanning range, and the duty cycle can be close to 50%; however, the limitations of the scanning speed and scanning range of the galvano scanner make a megahertz OCT impossible. Using a polygonal scanner as the streak scanner may sufficiently resolve this problem since it can achieve linear and fast-streak scanning. Furthermore, unlike the back-and-forth scanning style for both the galvano scanner and resonant scanner, the unidirectional scanning of the polygonal scanners allows a duty cycle of >50%. Nonetheless, the frame rate of the camera used in this work was too fast, and the frequency of the resonant scanner rate was not able to match the camera. The A-scan rate of this OCT technique can be further increased by replacing the streak scanner with a polygonal scanner. These three types of scanners are compared in scanning speed as shown in Table 1. For instance, a polygonal mirror with a clear aperture of 10 mm at 45 deg incident angle can achieve a higher repetition rate (2 KHz) and larger angular-scan range (24 deg optical angle) than we now have, which ensures that the entire camera sensor is covered.

We also noticed that the maximum scanning range of the resonant scanner used in this work is large enough for a camera with a larger sensor. A demonstration Pco.dimax camera from Cooke Corporation (2016×2016 pixels, 1000 frames/s) was tested in

our system: It replaced the Y4 camera. The same sample power was used, but the scanning range of the resonant scanner was increased to match the larger sensor. By setting a window of 1024×2016 pixels and an exposure time of 500 μs, the camera was operated at 1000 frames/s. The short aspect (1024 pixels) was set parallel to interference spectrum. Thus, 2,016,000 A-scans were obtained in 1 s. Day-3 chick embryos were scanned by this new system, and the results are shown in Fig. 9. Since its pixel size was 11 μm, and the height of the window was smaller than that of the Y4, there was a truncation in the spectrum. And, because the width of the sensor window was larger than that of the Y4 camera, there was an additional SNR drop due to lens aberrations at two sides of the B-scan as described in Sec. 3.1. But, the increase of A-scans per B-scan with current resonant scanner-based SM-FDOCT was demonstrated.

From SNR analysis, we can see that, generally, RIN noise will gradually dominate the total noise if the detection bandwidth increases further (i.e., increasing the A-scanning rate). This phenomenon will harm the sensitivity of the system with a larger detection bandwidth. However, when a camera with low noise is used, shot-noise-limited detection can be kept by reducing N_{ref}. Another solution for this problem is to use the multichannel design, which can keep the total A-scan rates while reducing the detection bandwidth.

5 Conclusions

We have demonstrated the design of a resonant scanner-based streak-mode FD-OCT and its application in ultrahigh-speed biological tissue imaging. Furthermore, in this technique, we have shown that the effect of the streak scanning is the change of the integration time window from rect(t/T) in conventional FD-OCT to prolonged $H(t)$ in streak mode FD-OCT. The prolonged integration time induces a larger SNR drop when samples are measured with axial or transverse motion compared with conventional FD-OCT. However, with sharp spectrum ($a/w_1 > 2$), this difference is negligible when sample motion is small ($k_0 \Delta z \ll 1$, $\Delta x/w_0 \ll 1$). In SM-FDOCT, aberrations result in SNR degradation at two sides of the B-scan, which may be improved by additional aberration correction. The outflow tract of HH19 chick hearts were imaged using this method at 1,016,000 A-scans/ps, and preliminary 2-M OCT data were obtained with another demo camera. The results demonstrated that this technique has the potential for MHz OCT imaging. Due to its high temporal resolution, it is suitable for cross-sectional imaging of high speed dynamic biomedical processes.
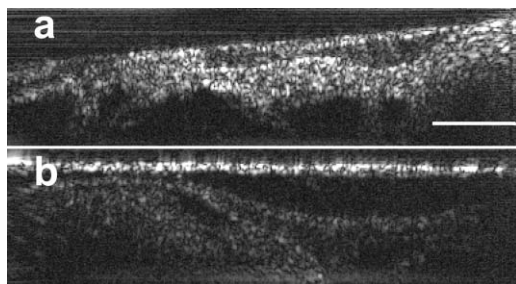
Fig. 9 Preliminary OCT images of day 3 chick embryos from a SM-FDOCT using a demo Pco.dimax camera. (a) and (b): results from different embryos. The scale bar is 200 μm.

Acknowledgments

References

1. W. Wieser, B. R. Biedermann, T. Klein, C. M. Eigenwillig, and R. Huber, "Multi-Megahertz OCT: High quality 3D imaging at 20 million A-scans and 4.5 GVoxels per second," *Opt. Express* **18**, 14685–14704 (2010).
2. A. H. Dhalla, J. V. Migacz, and J. A. Izatt, "Crosstalk rejection in parallel optical coherence tomography using spatially incoherent illumination with partially coherent sources," *Opt. Lett.* **35**, 2299–2301 (2010).
3. J. K. Ranka, R. S. Windeler, and A. J. Stentz, "Visible continuum generation in air-silica microstructure optical fibers with anomalous dispersion at 800 nm," *Opt. Lett.* **25**, 25–27 (2000).
4. I. Hartl, X. D. Li, C. Chudoba, R. K. Ghanta, T. H. Ko, J. G. Fujimoto, J. K. Ranka, and R. S. Windeler, "Ultrahigh-resolution optical coherence tomography using continuum generation in an air-silica microstructure optical fiber," *Opt. Lett.* **26**, 608–610 (2001).
5. S. H. Yun, G. J. Tearney, B. E. Bouma, B. H. Park, and J. F. de Boer, "High-speed spectral-domain optical coherence tomography at 1.3 mu m wavelength," *Opt. Express* **11**, 3598–3604 (2003).
6. N. Nassif, B. Cense, B. H. Park, S. H. Yun, T. C. Chen, B. E. Bouma, G. J. Tearney, and J. F. de Boer, "*In vivo* human retinal imaging by ultrahigh-speed spectral domain optical coherence tomography," *Opt. Lett.* **29**, 480–482 (2004).
7. B. Potsaid, I. Gorczynska, V. J. Srinivasan, Y. L. Chen, J. Jiang, A. Cable, and J. G. Fujimoto, "Ultrahigh speed Spectral/Fourier domain OCT ophthalmic imaging at 70000 to 312500 axial scans per second," *Opt. Express* **16**, 15149–15169 (2008).
8. B. Grajciar, M. Pircher, A. F. Fercher, and R. A. Leitgeb, "Parallel Fourier domain optical coherence tomography for in vivo measurement of the human eye," *Opt. Express* **13**, 1131–1137 (2005).
9. M. V. Sarunic, S. Weinberg, and J. A. Izatt, "Full-field swept-source phase microscopy," *Opt. Lett.* **31**, 1462–1464 (2006).
10. S. Bourquin, A. D. Aguirre, I. Hartl, P. Hsiung, T. H. Ko, J. G. Fujimoto, T. A. Birks, W. J. Wadsworth, U. Bunting, and D. Kopf, "Ultrahigh resolution real time OCT imaging using a compact femtosecond Nd : Glass laser and nonlinear fiber," *Opt. Express* **11**, 3290–3297 (2003).
11. Y. M. Wang, I. Tomov, J. S. Nelson, Z. P. Chen, H. Lim, and F. Wise, "Low-noise broadband light generation from optical fibers for use in high-resolution optical coherence tomography," *J. Opt. Soc. Am. A Opt. Image Sci. Vis.* **22**, 1492–1499 (2005).
12. M. Nishiura, T. Kobayashi, M. Adachi, J. Nakanishi, T. Ueno, Y. Ito, and N. Nishizawa, "*In vivo* ultrahigh-resolution ophthalmic optical coherence tomography using Gaussian-shaped supercontinuum," *Jpn. J. Appl. Phys.* **49**, 0127011 (2010).
13. R. Leitgeb, C. K. Hitzenberger, and A. F. Fercher, "Performance of fourier domain vs. time domain optical coherence tomography," *Opt. Express* **11**, 889–894 (2003).
14. A. M. Rollins and J. A. Izatt, "Optimal interferometer designs for optical coherence tomography," *Opt. Lett.* **24**, 1484–1486 (1999).
15. G. Häusler and M. W. Lindner, "'Coherence radar' and 'Spectral radar'—new tools for dermatological diagnosis," *J. Biomed. Opt.* **3**, 21–31 (1998).
16. S. H. Yun, G. J. Tearney, J. F. de Boer, and B. E. Bouma, "Motion artifacts in optical coherence tomography with frequency-domain ranging," *Opt. Express* **12**, 2977–2998 (2004).